JMEPEG (2006) 15:161-171
DOI: 10.1361/105994906X95814

1059-9495/$19.00

Machining of Depleted Uranium Using Coated Cutting Tools

M.J. Jackson and G.M. Robinson

(Submitted November 4, 2005; in revised form January 2, 2006)

The machining of depleted uranium and its alloys are discussed in this article. Traditionally, these materials have been machined, with limited success, using uncoated cutting tools. New developments in titanium-based coatings such as cation-substituted $Ti_{1-x-y-z}Al_xCr_yY_2N$ alloys, with $y = 0.03$ and $z = 0.02$, have been shown to offer enhanced high-temperature oxidation resistance compared with the presently used TiN and $Ti_{1-x}Al_xN$ films that are deposited to cutting tool surfaces. Layers (3 μm thickness) were deposited by unbalanced magnetron sputter (UBM) deposition to small-grain WC-Co unused cutting tools that had been ion-etched in situ using a steered Cr-metal-ion cathodic arc (CA) discharge at an Ar pressure of 6×10^{-4} mbar (0.45 mTorr). The metal ion etching promoted initial local epitaxy on individual substrate grains while the overall film texture evolved through competitive growth to a (111) plane in $Ti_{0.44}Al_{0.53}Cr_{0.03}N$ alloys and (200) plane in $Ti_{0.43}Al_{0.52}Cr_{0.03}Y_{0.02}N$ alloys. Although $Ti_{0.04}Al_{0.53}Cr_{0.03}N$ layers exhibited a columnar microstructure that was similar to that previously observed in $Ti_{1-x}Al_xN$ alloys, the addition of 2 mol% YN resulted in significant grain refinement, giving rise to an equiaxed structure. The Knoop microhardness of $Ti_{0.43}Al_{0.52}Cr_{0.03}Y_{0.02}N$ alloys was $HK_{0.025} = 2700$ kg/mm compared with 2400 kg/mm for $Ti_{0.44}Al_{0.53}Cr_{0.03}N$ alloys. The onset of rapid oxidation, as determined from thermogravimetric measurements, ranged from ≈600 °C for TiN; to 870 °C for $Ti_{0.466}Al_{0.54}N$; to 920 °C for $Ti_{0.44}Al_{0.53}Cr_{0.03}N$; to 950 °C for $Ti_{0.43}Al_{0.522}Cr_{0.03}Y_{0.02}N$. Machining experiments indicated that cutting tool life is improved significantly using Y-doped Ti-based coatings when machining uranium alloys.

Keywords	depleted uranium, machining, titanium-coated cutting tools, yttrium

1. Introduction

1.1 Uranium and Its Alloys

There are three classes of uranium alloys. These alloys are described as:

- Dilute alloys containing less than 0.4 wt.% of alloying elements
- Intermediate alloys containing between 0.4 and 4 wt.% of alloying elements
- Stainless alloys containing more than 4 wt.% of alloying elements

Uranium consists of an orthorhombic α uranium matrix, with carbides and oxides as the principal inclusions. The alloying elements used include Ti, which makes uranium hard, and Nb, which makes uranium corrosion-resistant. Depleted uranium and uranium alloys are used in nuclear weapons, calorimeter plates, ballistic penetrators, radiation shielding, counterweights, and gyroscope rotors. The machinability of uranium is affected by the following characteristics:

- Shape memory
- Nonisotropic coefficient of thermal expansion
- Pyrophoric, toxic, and radioactive properties

Shape memory is the property of a material to return to its original shape after a change in temperature and is more prevalent in alloyed uranium than in unalloyed uranium. The nonisotropic coefficient of thermal expansion causes the material to distort under a thermal influence. This means that the material expands in two crystallographic directions rather than in three when subjected to a thermal influence. Unalloyed uranium expands in two principal directions and contracts in the third. During machining, the cutting tool must be kept sharp and the temperature of the material must be kept as low as possible. Uranium and its alloys can generally be machined to tolerances within the range of a standard lathe. Tolerances on the order of 8 μm are not uncommon. However, cutting tools must remain sharp to produce accurate tolerances.

1.2 Wear of Cutting Tools

Cutting tool wear is the product of a combination of load factors on the cutting edge of the tool (Ref 1). Wear is the result of interactions among the tool, the workpiece material, and machining conditions. The load factors are mechanical, thermal, chemical, and abrasive.

Apart from the static components of mechanical loads, there are various dynamic components arising from chip formation itself. Metal cutting generates a lot of heat on the face of the chip and on the flank of the insert. Thermal loads are considerable on the tool material, and during interrupted machining operations the thermal load pulsates, thus leading to thermal fatigue of the tool material. The typical wear zones on the

This paper was presented at the fourth International Surface Engineering Congress and Exposition held August 1-3, 2005 in St. Paul, MN.

M.J. Jackson and **G.M. Robinson,** Center for Advanced Manufacturing, College of Technology, Purdue University, West Lafayette, IN 47907. Contact e-mail: jacksomj@purdue.edu.

cutting edge are shown in Fig. 1 and 2. The formation of a chip means that a fresh metal interface is continuously produced, and is forced at very high pressure and temperature along the tool. The zones produced make it an attractive environment for diffusion and chemical reactions to occur.

As a result of the load factors exerted on the cutting tool edge, a few basic mechanisms dominate metal cutting. These mechanisms are:

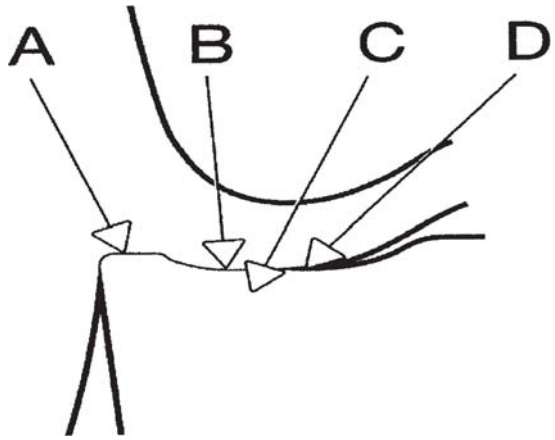

Fig. 1 Wear zones on the cutting tool caused by chip formation (Ref 1)

- *Diffusion wear:* affected by chemical loading on the tool, which is controlled by the metallurgical composition of the tool and coating material
- *Abrasive wear:* affected by the hardness of the tool material, which is controlled by the carbide content of the cutting tool material
- *Oxidation wear:* causes gaps to occur in coated films and results in a loss of the coating at elevated temperatures
- *Fatigue wear (static or dynamic):* a thermomechanical effect that leads to breakdown of the edges of the cutting tool
- *Adhesion wear:* occurs at low machining temperatures on the chip face of the tool, and leads to the formation of a built-up-edge, and to continual edge breakdown and subsequently breakdown of the tool edge itself

The classification of cutting tool wear is shown in Fig. 3. The criterion of the machining (i.e., removal rate, surface roughness, tool life, and chip control) depends on the development of tool wear. Figure 4 shows the first three types of tool wear, which are known as flank wear, crater wear, and plastic deformation. Flank wear is caused by abrasive wear as the chip moves against the face of the cutting tool. This type of wear is normal and progressive. Crater wear is caused by a combination of abrasive and diffusion wear mechanisms. High tool hardness and high hot hardness of the tool minimize the tendency for crater wear to occur. Crater wear should be avoided

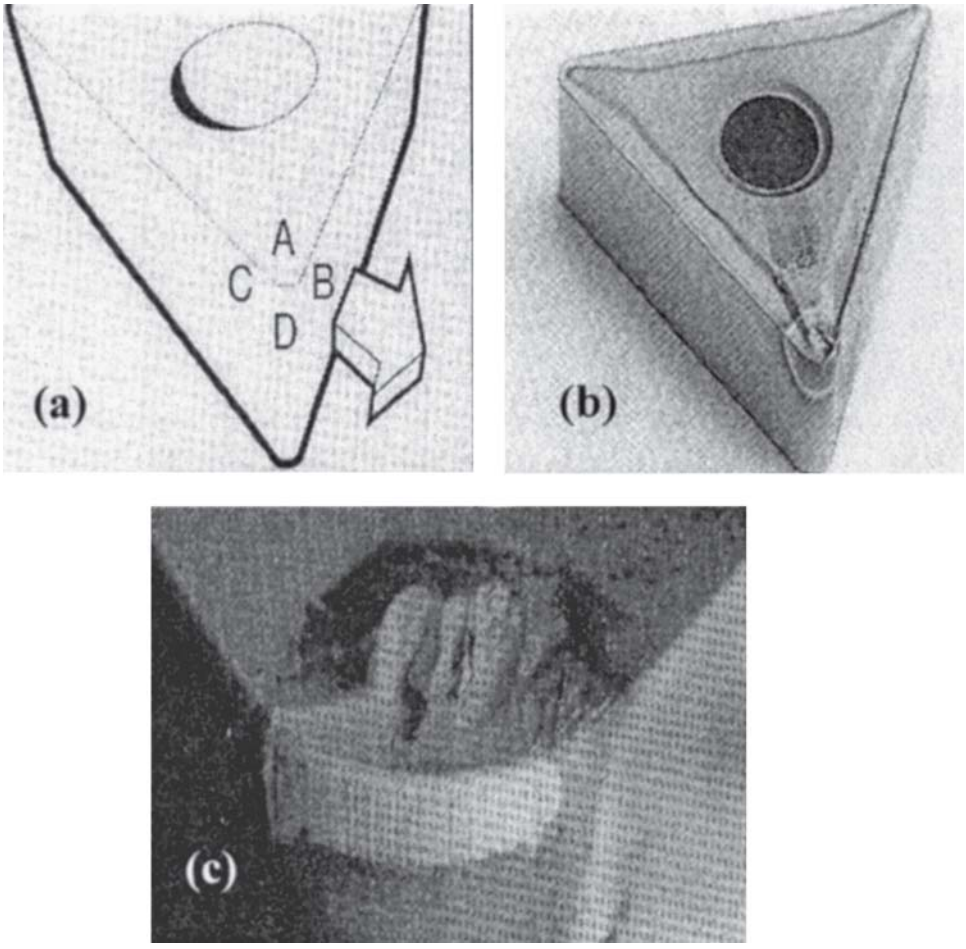

Fig. 2 (a) Areas of wear on the cutting tool insert shown in Fig. 1; (b) physical cutting tool insert showing worn edges described in (a); and (c) well-developed flank and crater wear at the nose of the insert (Ref 1)

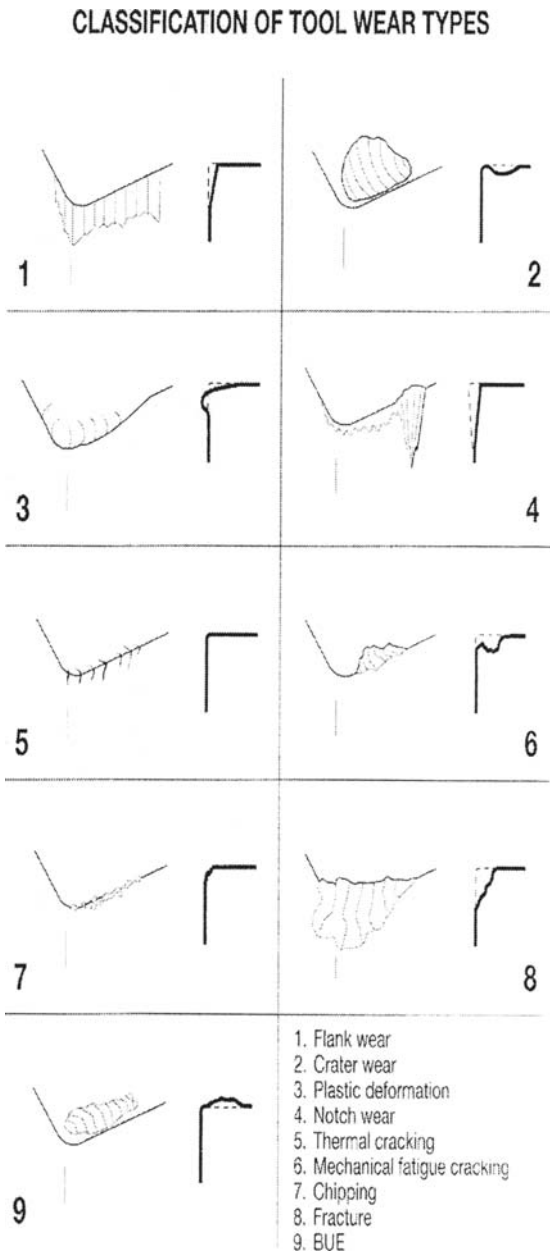

Fig. 3 Classification of cutting tool wear caused by a combination of different tool wear mechanisms (Ref 1)

as it changes the geometry of the tool and weakens the cutting edge.

Plastic deformation takes place as a function of high pressures and temperatures on the cutting tool. Figure 5 shows notch wear, thermal cracking, and mechanical fatigue cracking of the cutting tool.

Notch wear on the trailing edge is a type of adhesion wear but can also be caused by oxidation. The wear is localized at the end of the cut where air can penetrate the cutting zone. Notch wear on the leading edge is mechanical and weakens the cutting edge. Thermal cracking is a form of fatigue and is due to thermal cycling. Cracks form in the tool material, and the edge of the tool is lost through machining. Varying the chip thickness affects the cutting temperature at the chip-tool interface and can lead to the rapid breakdown of the tool material. Mechanical fatigue cracking takes place when cutting force

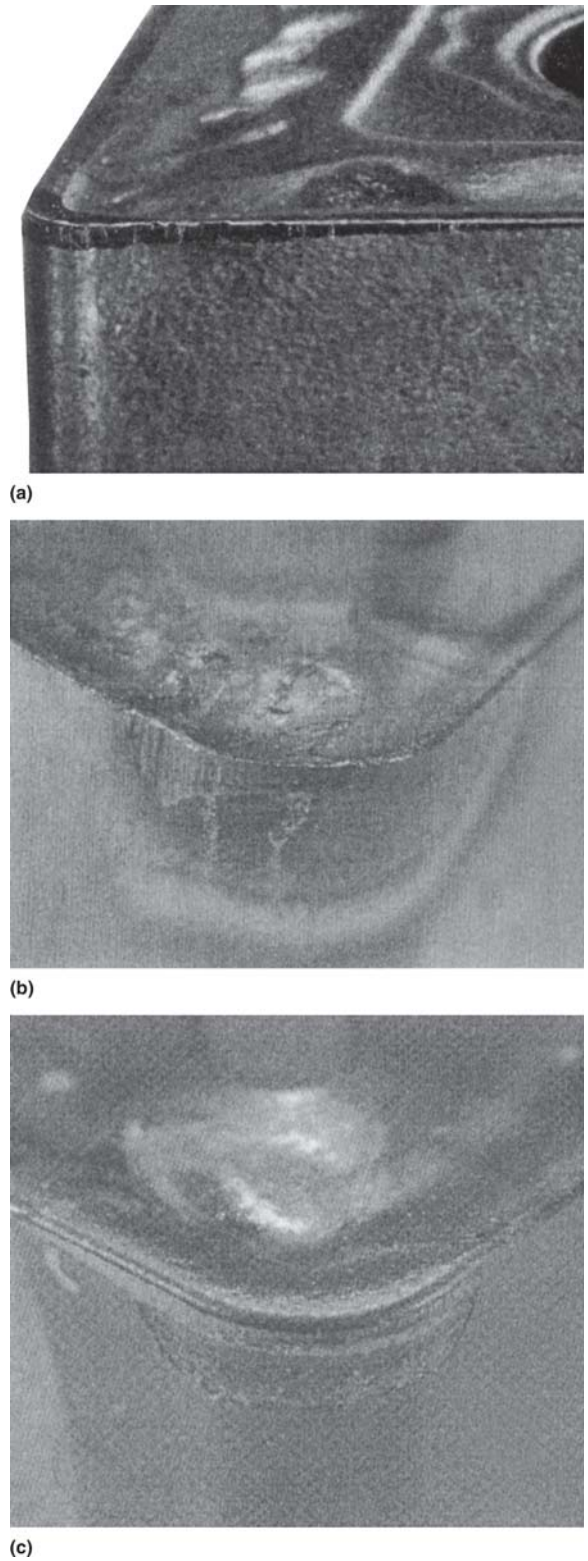

Fig. 4 Cutting tool wear types: (a) flank wear; (b) crater wear; and (c) plastic deformation (Ref 1)

shocks are excessive. Figure 6 shows the wear of the cutting edge caused by chipping, fracture, and the built-up edge. Chipping of the cutting edge is cyclic and is caused by the fatigue of the cutting tool due to intermittent cutting. Fracture is the catastrophic breakdown of the tool material and is caused by

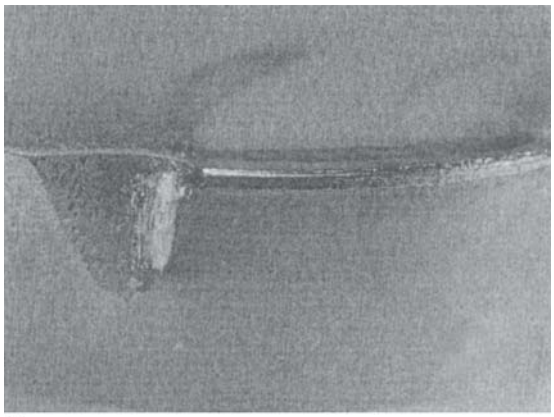

(a)

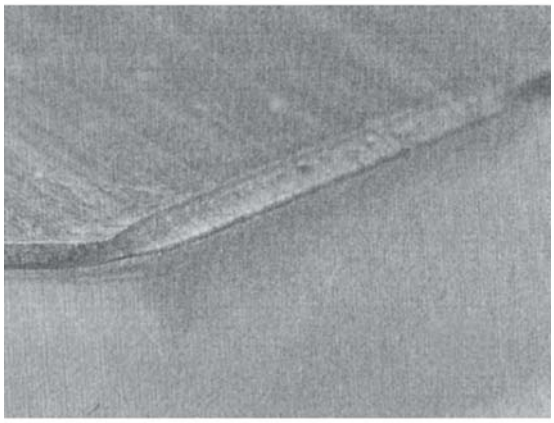

(b)

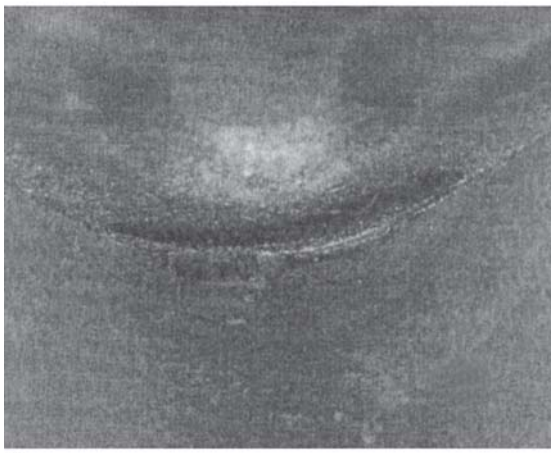

(c)

Fig. 5 Cutting tool wear types: (a) notch wear; (b) thermal cracking; and (c) mechanical fatigue cracking (Ref 1)

heavy cuts or very high cutting forces. Finally, the built-up edge changes the geometry of the cutting tool and leads to an increase in the level of the cutting force. When the built-up edge breaks off, the cutting tool force is reduced, which leads to a cycling of the load. The tool edge eventually breaks off.

1.3 Machining of Uranium Alloys

Uranium and its alloys are tough, soft, and tend to form a built-up edge. Carbide inclusions tend to make them abrasive

(a)

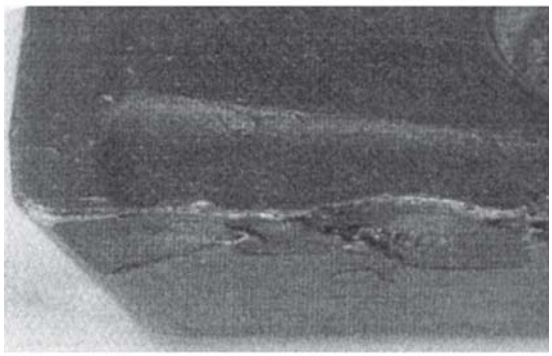

(b)

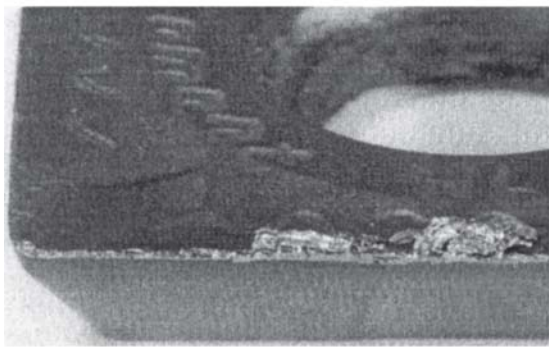

(c)

Fig. 6 Cutting tool wear types: (a) chipping; (b) fracture; and (c) built-up edge (Ref 1)

as well. Flank wear is the normal type of wear encountered during the machining of uranium alloys when using the correct machining parameters (Ref 2). The cutting edge appears to be mechanically worn, not chipped or notched. Traditionally, cutting tools that provide the best results for turning and facing uranium alloys and unalloyed uranium are uncoated grades of high TaC content having the nominal compositions (Ref 2):

- 74wt.%WC-20wt.%TaC-6wt.%Co
- 50wt.%TaC-44wt.%WC-6wt.%Co

The tools have positive rake angles between 5 and 12°. For harder alloys, WC inserts work better where abrasion, rather than heat at the tool tip, is the primary wear mechanism. In the past, machining with coated cutting tools has generally failed due to the cracking and excessive wear of the coating. High-TaC content tool inserts are preferred when machining unal-

Table 1 Typical machining parameters when turning and facing uranium alloys (Ref 2)

Variables	Roughing	Finishing
Depth of cut, mm	1.27-2.54	0.0025-012
Cutting speed, m/min	30-107	122
Feed, mm/revolution	0.15-0.2	0.05-0.1

loyed uranium because they can tolerate high levels of heat that is generated at the tool tip. However, higher TaC contents lower the hardness of the tools, leading to excessive wear of the tool edge. Typical machining parameters when turning and facing uranium alloys are shown in Table 1 (Ref 2).

1.4 Coated Cutting Tools

The initial investigations into the deposition and microstructural properties of metastable $Ti_{1-x}Al_xN$ coatings were first published over a decade ago (Ref 3-6). The principal reason for their increased use over TiN coatings in dry cutting and milling operations stems from enhanced high-temperature oxidation resistance. TiN oxidizes rapidly at temperatures above ≈600 °C to form a layer that is predominantly rutile TiO_2, which has a much larger molar volume than TiN and results in discontinuous spallation. In contrast, McIntyre et al. (Ref 7) showed that annealing $Ti_{0.5}Al_{0.5}N$ in oxygen gives rise to the formation of a stable passive oxide double layer, with the upper layer being Al-rich and the lower layer being Ti-rich, with no measurable nitrogen in either. Inert marker experiments demonstrated that oxidation of $Ti_{0.5}Al_{0.5}N$ proceeds by the simultaneous outward diffusion of Al to the oxide-vapor interface and inward diffusion of O to the oxide-nitride interface.

A potential approach to further improving high-temperature performance is the addition of small concentrations of alloying components that are known to provide even higher oxidation resistance (Ref 8). In this article, the first results on the microstructure and oxidation resistance of the $Ti_{1-x-y-z}Al_xCr_yY_2N$ films deposited, using a combined CA/UBM deposition process, are reported (Ref 9, 10). This article also describes the improvement in cutting tool life during dry machining operations when using a series of coated tool inserts to machine uranium alloys, which suggests that Y-doped coatings may have a beneficial effect on cutting tool life compared with TiN and TiAlN coatings.

2. Experimental Procedure

2.1 Deposition of Coatings to Cutting Tools

All films were deposited in a Hauzer Techno Coating Europe B.V. HTC 1000-4 (Holland, The Netherlands) combined CA/UBM system (Ref 9). The growth chamber contains four 60 × 19 × 1.2 cm vertically mounted targets (two opposing pairs, each separated by 100 cm), which can function in either the CA or UBM mode. The base pressure of the system is less than 10^{-5} mbar (7×10^{-6} torr). Three radiant heater arrays allow independent closed-loop control of the growth temperature (450 °C) using two chromel-alumel thermocouples attached to the surface of dummy substrates. For this study, the following targets (>99.8% pure) were used: a hot isostatic pressed Cr plate; two cast $Ti_{0.5}Al_{0.5}$ plates; and a forged $Ti_{0.48}Al_{0.48}Y_{0.04}$ plate. Sputtering was carried out in mixed N_2 (99.999%) and Ar (99.999%) discharges with the Ar flow maintained constant at 200 standard cubic centilitres/min (sccm) while the N_2 flow was regulated to maintain the total pressure at 3.4×10^{-3} mbar (2.5 mtorr).

The inserts used in these experiments were fine-grain cobonded WC inserts, polished to an average peak-to-valley roughness of $R_a = 10$ nm, cleaned as described by Petrov et al. (Ref 10), and mounted in a substrate holder with a three-axis planetary rotation table. The average target-to-substrate distance was 25 cm. Immediately prior to deposition, the substrates were subjected to −1.2 kV Cr-steered-arc metal-ion etching for 20 min at a total pressure of 6×10^{-4} mbar (0.45 mtorr). Cr was chosen as an ion etchant to suppress droplet deposition on the substrate (Ref 11). A 0.2 μm thick $Ti_{1-x-y}Al_xCr_yN$ base-layer was then deposited by UBM, in which the power to the two $Ti_{0.5}Al_{0.5}$ targets P_{TiAl} was 8 kW each, while $P_{Cr} = 0.5$ kW and $P_{TiAlY} = 0$. Power to the $Ti_{0.48}Al_{0.48}Y_{0.04}$ was then set at 8 kW to deposit 3 μm thick $Ti_{1-x-y-z}Al_xCr_yY_zN$ films. The properties of $Ti_{1-x-y-z}Al_xCr_yY_zN$ were compared with $Ti_{1-x-y}Al_xCr_yN$ layers of equivalent thickness that were deposited under the same conditions as the base-layer, and with $Ti_{1-x}Al_xN$ ($P_{Cr} = 0$) layers that were deposited using three $Ti_{0.5}Al_{0.5}$ targets operated at $P_{TiAl} = 8$ kW. In all cases, the substrate bias during film growth was maintained at a constant −75 V.

Surface morphologies of as-deposited and annealed samples were examined using scanning electron microscopy (SEM), while microstructures and phase compositions of films and film-substrate interfaces were determined using a combination of x-ray diffraction (XRD) and cross-sectional transmission electron microscopy (XTEM). The XTEM samples were prepared by mechanical thinning and ion milling, as described by Petrov et al. (Ref 10). Area-averaged elemental depth profiles were measured by 2 MeV He Rutherford backscattering spectroscopy (RBS) and secondary neutral mass spectrometry (SNMS) using a 16 keV Ga^+ primary beam. Local compositional profiles were investigated using energy-dispersive x-ray (EDX) analyses of XTEM samples in a Vacuum Generators (Manchester, U.K.) HB5 scanning transmission electron microscope (STEM) equipped with a field-emission source and operated at 100 kV. During STEM analyses, samples were traversed with respect to a stationary electron beam focused to a diameter of ≈1 nm, and x-ray spectra were collected at a takeoff angle of 40°. Corrections for atomic number were carried out using the MAGIC-V computer code (Ubisoft, Austin, TX) (Ref 12). Oxidation rates in air were assessed by thermogravimetric analyses (TGA) in isothermal mode (800-950 °C for up to 5 h) and linear-temperature-ramp mode (400-1000 °C at 1 °C/min). Knoop microhardness values were determined using a load of 25 × *g*.

2.2 Machining Experiments

Machining experiments were performed to assess the life of newly developed Ti-based coated tools. The assessment of machinability used in these experiments pertains to the development of Taylor's tool life equations for uncoated and coated cutting tools. Taylor's tool life equation is stated as:

$$VT^n = C \quad \text{(Eq 1)}$$

where V is the cutting speed in meters per minute, T is the tool life in minutes, n is an exponent that is dependent upon the machining conditions and the tool and workpiece composi-

tions, and C is a constant. For each tool life equation generated, a sample of the metal is turned at a specific cutting speed, and the time it takes to wear 0.3 mm of the flank face of the insert away from the cutting tool is noted and used in the calculation. For the machining of uranium alloys in this study, a computerized numerically controlled lathe was used to vary the cutting speed. An Emco Maier (Columbus, OH) CNC lathe was used to turn 25.4 mm round bars of uranium alloy that had a measured surface roughness of 25 μm. A roughing cut was used with the parameters shown in Table 1. A maximum cut of 2.54 mm was used to produce a thick chip. Water coolant was applied to the chips as they collected in the chip tray. This experiment was performed so as not to ignite the chips after they were deposited into the chip tray. "Dry" machining of the metal was performed to confirm or refute the effectiveness of the coated tool inserts. The uncoated cutting tool inserts were composed of 94 wt.% WC bonded with a 6 wt.% Co binder. The coated cutting tools were supplied with a superlattice coating that was composed of 1000 deposited layers to form a coating thickness of 3 μm. The alloy used for the machining experiments was an intermediate uranium alloy with 0.75 wt.% Ti content, which is usually used for armor-piercing applications. The maximum feed rate was set at 0.2 mm per revolution of the spindle. The tools were initially sharp and were not previously used in any other application. The tool inserts were coated at the Bodycote-SHU facility, which is housed within the Materials Research Institute at Sheffield Hallam University. The initial cutting speed used for the experiments was set at 30 m/min. The tool life was measured by inspecting the cutting tool until 0.3 mm of the flank had worn away. Further increments of cutting speed were made until a maximum cutting speed of 70 m/min had been achieved.

3. Results and Discussion

3.1 Microstructure, Composition, and Properties of As-Deposited Layers

Elemental analysis by RBS and STEM-EDX revealed that the $Ti_{1-x}Al_xN$, $Ti_{1-x-y}Al_xCr_yN$, and $Ti_{1-x-y-z}Al_xCr_yY_zN$ films were stoichiometric with mean N/metal ratios 1 ± 0.03 and compositions of $Ti_{0.46}Al_{0.54}N$, $Ti_{0.44}Al_{0.53}Cr_{0.03}N$, and $Ti_{0.43}Al_{0.52}Cr_{0.03}Y_{0.02}N$, respectively.

XRD θ-2θ scans showed that as-deposited $Ti_{0.44}Al_{0.53}Cr_{0.03}N$ and $Ti_{0.43}Al_{0.52}Cr_{0.03}Y_{0.02}N$ layers were single phase in the B1-NaCl structure with lattice parameters a_o of 0.4170 and 0.4220 nm, respectively. Comparison of integrated peak intensities showed that $Ti_{0.44}Al_{0.53}Cr_{0.03}N$ alloys exhibit a strong (111) preferred orientation with an I_{111}-to-I_Σ intensity ratio of 0.84; however, the incorporation of 2 mol% YN resulted in a (200) texture with an I_{002}-to-I_Σ intensity ratio of 0.67. For comparison, the (111) and (200) intensity ratio values for randomly oriented TiN (Ref 13) were 0.28 and 0.37, respectively. Peak widths were found to increase significantly with the addition of YN. For example, the full-width-at-half-maximum intensity of the $Ti_{0.43}Al_{0.52}Cr_{0.03}Y_{0.02}N$ (111) peak was larger by a factor of 5 (1 versus 0.2°) than that of $Ti_{0.44}Al_{0.53}Cr_{0.03}N$. From the XTEM analyses discussed below, this was primarily due to the strong effect of Y on grain refinement.

Figure 7(a) and (b) shows bright-field XTEM images and selected-area electron diffraction (SAED) patterns from as-deposited $Ti_{0.44}Al_{0.53}Cr_{0.03}N$ and $Ti_{0.43}Al_{0.52}Cr_{0.03}Y_{0.02}N$ films on stainless steel. Examination of the film-substrate interface reveals local epitaxy on underlying substrate grains that evolves into competitive columnar growth at a thickness greater than 100 to 150 nm. The formation of a similar interfacial microstructure was described in detail by Petrov et al. (Ref 10) for the case of $Ti_{1-x-y}Al_xNb_yN$ alloys deposited on steel substrates following $Ti_{0.50}Al_{0.50}$ CA ion etching. In $Ti_{0.44}Al_{0.53}Cr_{0.03}N$ films, the individual columns are typically single grains giving rise to uniform XTEM contrast over extended column lengths. The SAED image in Fig. 7(a), obtained with a 0.5 μm diameter aperture focused at the middle of the film, shows a B1-NaCl structure pattern with rings of spots that are consistent with a relatively large grain size.

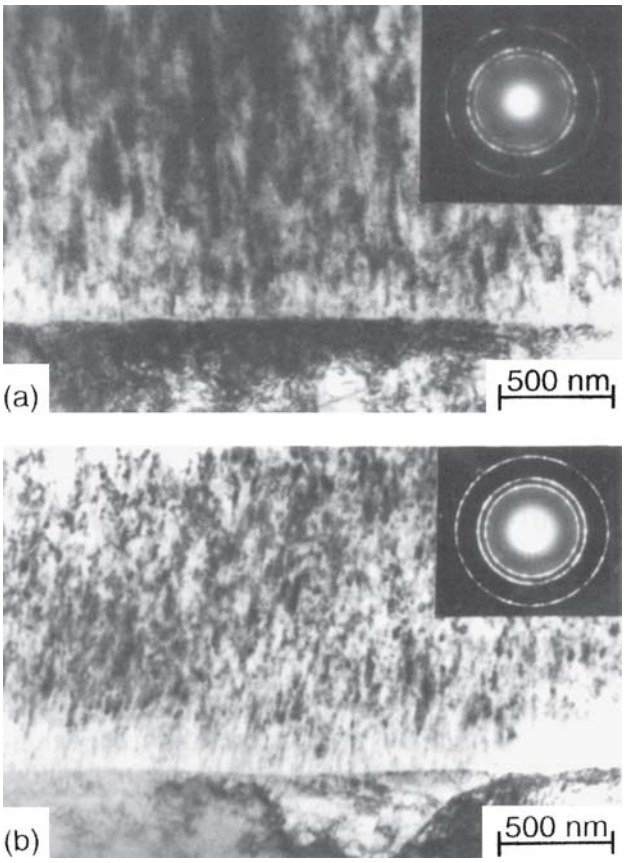

Fig. 7 XTEM bright-field images and SAED patterns from as-deposited (a) $Ti_{0.44}Al_{0.53}Cr_{0.03}N$ alloy and (b) $Ti_{0.43}Al_{0.52}Cr_{0.03}Y_{0.02}N$ alloy layers on steel substrate (courtesy of Professor Munz, Sheffield Hallam University, U.K.)

$Ti_{0.43}Al_{0.52}Cr_{0.03}Y_{0.02}N$ samples exhibit a transition, above the base layer, to much less pronounced columnar growth with nearly equiaxed grains. The addition of YN resulted in disruption, through continuous renucleation, of local epitaxy on individual columns. Similar microstructures have been observed to form when renucleation was generated in TiN (Ref 14) films by excessive ion-irradiation damage, and in $Ti_{1-x}Al_xN$ (Ref 15) metastable alloys by wurtzite-AlN phase precipitation during growth. In the present experiments, the renucleation is attributed to Y surface segregation during deposition. Consistent with the small grain size, the SAED pattern in Fig. 7(b) exhibits broad continuous rings of approximately uniform intensity.

The Knoop microhardness for $Ti_{0.46}Al_{0.54}N$ and $Ti_{0.44}Al_{0.53}Cr_{0.03}N$ was $HK_{0.025} = 2400\ kg/mm^2$, which is consistent with the values from previous reports (Ref 6) for

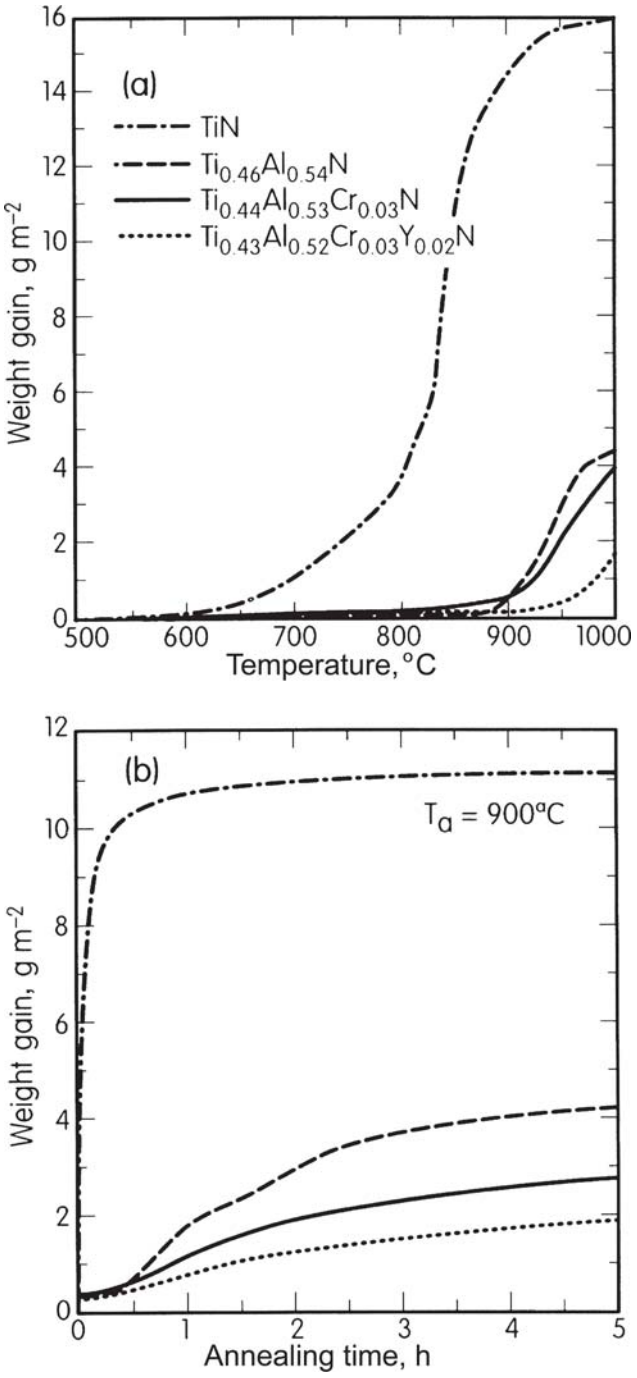

Fig. 8 Thermogravimetric oxidation rate measurements in air during (a) a linear-temperature ramp at 1 °C/min and (b) an isothermal anneal at 900 °C (courtesy of Professor Munz, Sheffield Hallam University, U.K.)

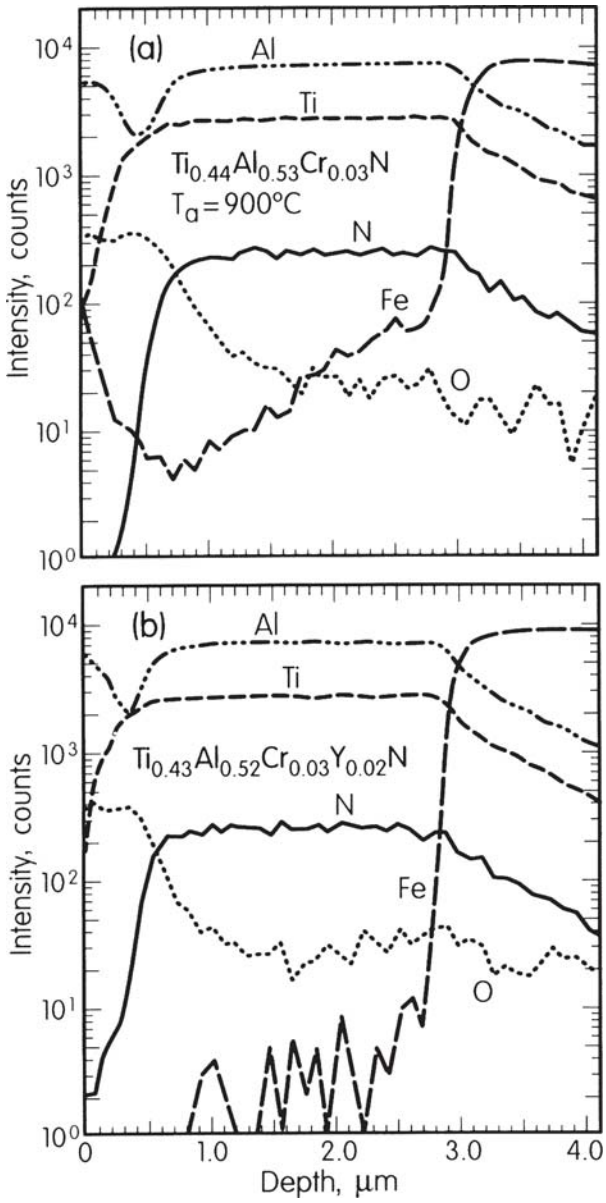

Fig. 9 SNMS profiles from (a) $Ti_{0.44}Al_{0.53}Cr_{0.03}N$ and (b) $Ti_{0.43}Al_{0.52}Cr_{0.03}Y_{0.02}N$ alloys annealed for 1 h at 900 °C (courtesy of Professor Munz, Sheffield Hallam University, U.K.)

$Ti_{0.5}Al_{0.5}N$. The incorporation of YN increased $HK_{0.025}$ to 2700 kg/mm^2. The surface roughness, measured using a stylus profilometer, was R_a = 0.038 to 0.040 μm for all films. The VDI Rockwell-C (Rockwell Scientific, Thousand Oaks, CA) indentation adhesion evaluation revealed an indent quality (Ref 16) of 1, indicating excellent adhesion.

3.2 Oxidation Behavior

Figure 8(a) and (b) are plots of TGA oxidation rate measurements for TiN, $Ti_{0.46}Al_{0.54}N$, $Ti_{0.44}Al_{0.53}Cr_{0.03}N$, and $Ti_{0.43}Al_{0.52}Cr_{0.03}Y_{0.02}N$ layers. The onset for the rapid oxidation of TiN during 1 °C/min thermal ramping (Fig. 8a) occurs at $T_{ox} \approx$ 600 °C, while the T_{ox} for $Ti_{0.46}Al_{0.54}N$, $Ti_{0.44}Al_{0.53}Cr_{0.03}N$, and $Ti_{0.43}Al_{0.52}Cr_{0.03}Y_{0.02}N$ alloys increases to ≈870, 920, and 950 °C, respectively. Isothermal measurements at 900 °C (Fig. 8b) also show that alloying dramatically enhances the oxidation resistance. The data not only confirm the superior oxidation resistance of $Ti_{1-x}Al_xN$ over TiN (Ref 5, 7), but also demonstrate that the successive addition of small amounts of CrN and YN to $Ti_{1-x}Al_xN$ provide further significant improvements.

Oxidation reaction paths were determined using a combination of SNMS, SEM, XTEM, and STEM-EDX analyses. Figure 9(a) and (b) are SNMS profiles from $Ti_{0.44}Al_{0.53}Cr_{0.03}N$ and $Ti_{0.43}Al_{0.52}Cr_{0.03}Y_{0.02}N$ alloys that were annealed for 1 h at 900 °C. For clarity of presentation, only the major signals (N, O, Ti, Al, and Fe) are plotted. Both samples exhibit a two-

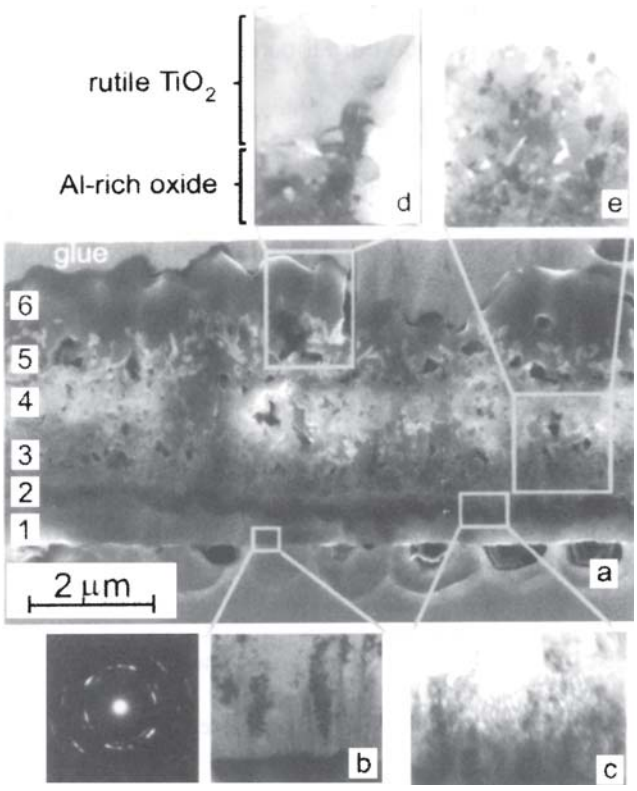

Fig. 10 A collage of SEM and XTEM images from a $Ti_{0.44}Al_{0.53}Cr_{0.03}N$ layer annealed for 1 h in air at 950 °C. (a) A large-scale SEM micrograph of the XTEM sample. (b-d) Higher resolution XTEM images of the indicated regions; SAED pattern corresponding to sublayer 1.

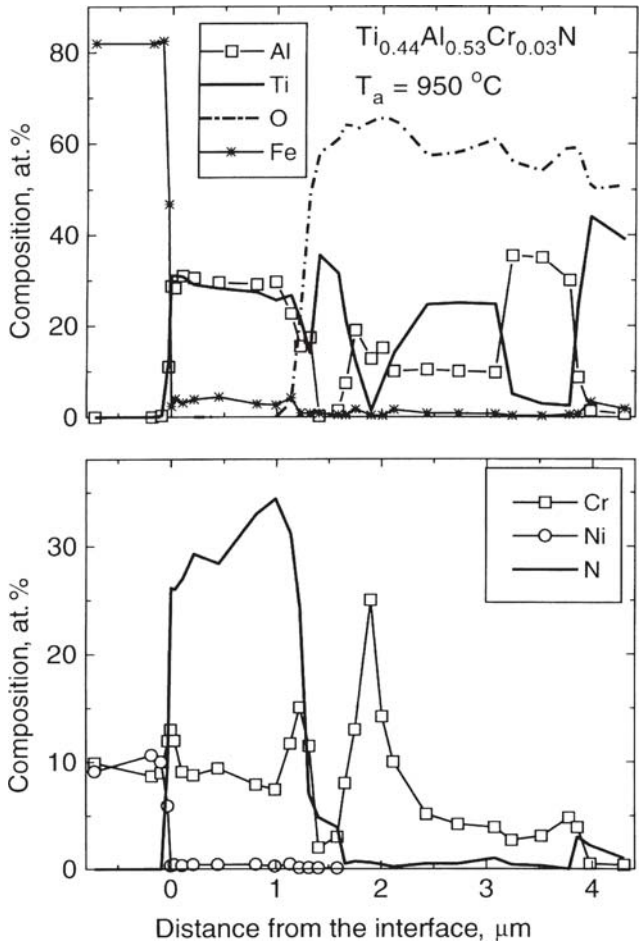

Fig. 11 STEM-EDX compositional depth profile through the cross-sectional sample shown in Fig. 10 (courtesy of Professor Munz, Sheffield Hallom University, U.K.)

layer, Al-rich zone followed by a Ti-rich (i.e., Al-depleted) oxidation zone similar to that reported (Ref 7) for the initial stages of $T_{0.5}Al_{0.5}N$ oxidation. Figure 9 shows that the oxide bilayer thickness decreases from 0.8 to 0.6 μm with the addition of YN. In the case of $Ti_{0.44}Al_{0.53}Cr_{0.03}N$, the Fe substrate profile is markedly broadened, penetrating the entire nitride film and accumulating at the free surface. In contrast, no measurable Fe penetration is observed in the $Ti_{0.43}Al_{0.52}Cr_{0.03}Y_{0.02}N$ layers.

Figure 10 is a collage of SEM and XTEM images from a $Ti_{0.44}Al_{0.53}Cr_{0.03}N$ layer that was annealed for 1 h in air at a higher temperature of 950 °C. The large-scale SEM micrograph of the XTEM sample in Fig. 10(a) reveals massive oxidation together with the formation of micron-size voids in the substrate. The film region near the interface, which is marked as sublayer "1" in Fig. 10(a) and is shown at a higher resolution in the XTEM image in Fig. 10(b), exhibits a columnar structure similar to as-deposited nitride layers. The SAED pattern shows that this region remains an NaCl structure after annealing. The darker-contrast sublayer 2, which is magnified in Fig. 10(c), consisted of columnar nitride grains that are partially oxidized. The column boundaries are eroded and open as a result of cation out-diffusion. Above region 2, several oxide sublayers (sublayers 3–6) are visible with increasing grain size toward the free surface.

Figure 11 is a typical STEM-EDX compositional depth profile of the sample presented in Fig. 10, revealing a complex sequence of compositional modulations. Based upon the XTEM, SAED, and STEM results, together with previously detailed studies of $Ti_{0.5}Al_{0.5}N$ oxidation (Ref 7), the profiles in Fig. 11 can be interpreted as follows.

The top three sublayers correspond to those observed in $Ti_{0.5}Al_{0.5}N$ after prolonged annealing at $T_{ox} > 900$ °C (Ref 7). Large-faceted TiO_2 crystallites with a rutile structure (see upper part of Fig. 10a, d) have developed on top of the initially formed Al-rich/Ti-rich oxide bilayer through the massive out-diffusion of Ti. The oxide bilayer, which initially is fine-grained and continuous, has coarsened through recrystallization and becomes porous, as seen in Fig. 10. Thus oxygen can, at this stage, more rapidly access the oxidation front, where STEM-EDX profiles show the formation of a second Al-rich/Ti-rich oxide bilayer. The new feature at this second stage of oxidation is that Cr accumulates to ≈15 at.% at the lower interface, and 25 at.% at the upper interface of the second Ti-rich oxide sublayer. This is another indication of the out-diffusion of substrate species during annealing. Indeed, the content of Cr in the substrate near the film-substrate interface is significantly depleted (<10 at.% compared with the initial ≈18 at.%). The out-diffusion of Cr is directly related to the formation of voids in the substrate. The loss of Cr and Fe from the steel is the cause of the voids observed in the substrate near to the interface (Fig. 10a). Similar analyses were carried out on $Ti_{0.43}Al_{0.52}Cr_{0.03}Y_{0.02}N$ films that were annealed under identical conditions. The SEM micrograph in Fig. 12(a) shows that, compared with $Ti_{0.44}Al_{0.53}Cr_{0.03}N$, the film is still dense with

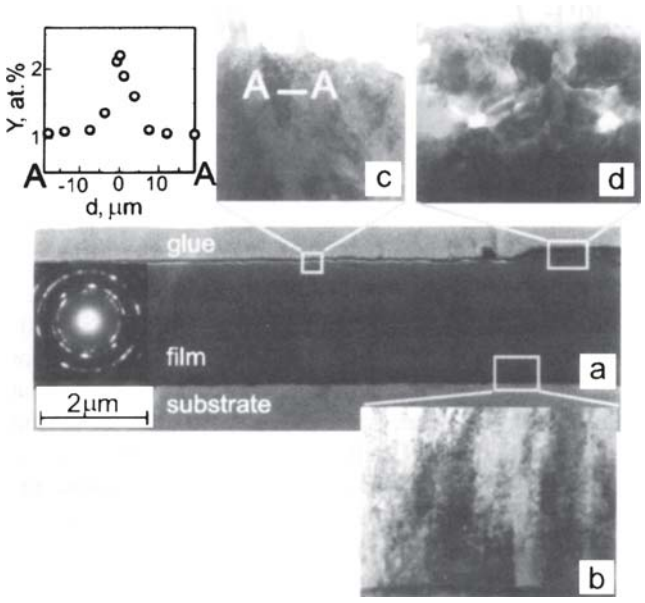

Fig. 12 A collage of SEM and XTEM images from a $Ti_{0.43}Al_{0.52}Cr_{0.03}Y_{0.02}N$ layer annealed for 1 h in air at 950 °C. (a) A large-scale SEM micrograph of the XTEM sample. (b–d) Higher-resolution XTEM images of the indicated regions; the SAED pattern corresponds to the nitride film. The inset shows the Y concentration from a STEM-EDX profile along the line A-A in (c) (courtesy of Professor Munz, Sheffield Hallam University, U.K.).

relatively little evidence of oxidation. The XTEM images of the interfacial region (Fig. 12b) and the upper region (Fig. 12c) of the annealed sample reveal that the film-substrate interface remains abrupt and that the $Ti_{0.43}Al_{0.52}Cr_{0.03}Y_{0.02}N$ microstructure is virtually unaffected by the anneal. The SAED patterns from the base-layer (not shown) and the bulk film are essentially identical to those from as-deposited layers. The microstructure of the oxide layer, shown in the XTEM micrograph in Fig. 12(d), exhibits a dense, partially crystalline surface overlayer with a thickness of between 100 and 150 nm and an underdense, although coarser (grain size ≈100 nm), polycrystalline underlayer. The total thickness of the oxide layer on $Ti_{0.43}Al_{0.52}Cr_{0.03}Y_{0.02}N$ is ≈0.4 μm compared with greater than 3 μm on $Ti_{0.44}Al_{0.53}Cr_{0.03}N$ after annealing for 1 h at 950 °C. Most of the oxide layer delaminated during XTEM sample preparation and is only visible in the upper right-hand corner of Fig. 12(a).

Figure 13 is a typical STEM-EDX compositional depth profile through the film-substrate interfacial region and the oxidized region of the $Ti_{0.43}Al_{0.52}Cr_{0.03}Y_{0.02}N$ sample shown in Fig. 12. The interface width (i.e., the distance over which the Fe, Al, and Ti signals change from 15 to 85% of their saturation values) remains the same as for the as-deposited samples (≈15 nm). The concentrations of Cr and Fe in the base-layer near the film-substrate interface are ≈12 and 5 at.%, respectively, and decrease rapidly in the bulk $Ti_{0.43}Al_{0.52}Cr_{0.03}Y_{0.02}N$ film. The profile through the oxidized region again shows an Al-rich/Ti-rich bilayer with CrO_x accumulation on both sides of the Ti-rich oxide layer. In this case, however, not only is the oxide bilayer much thinner, but the Cr concentration is substantially reduced (<10 at.% Cr). YO_x also accumulates at the interface between the Ti-rich and Al-rich oxide sublayers, but not at the lower Ti-rich oxide-nitride interface.

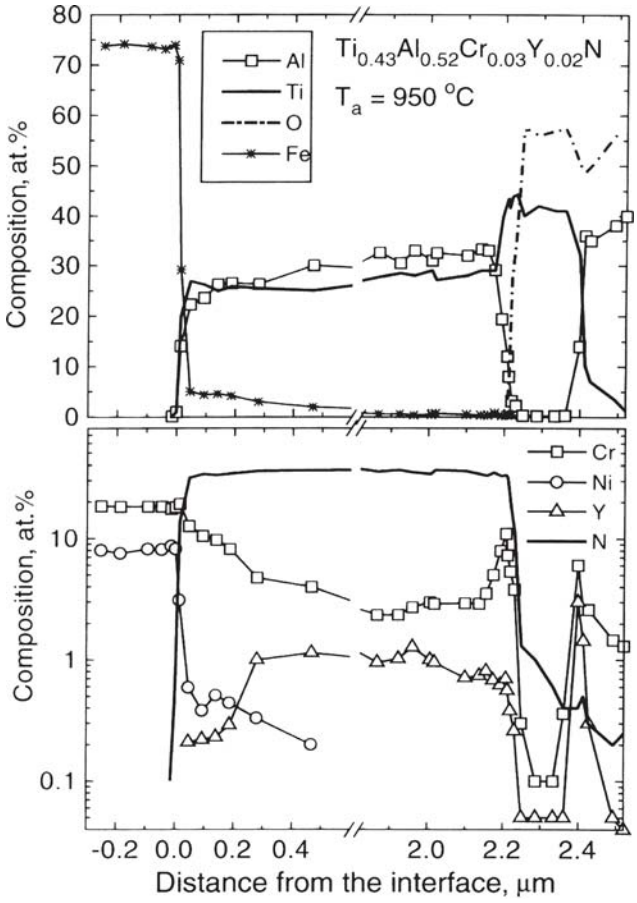

Fig. 13 STEM-EDX compositional depth profile through the interfacial and oxidized regions of the cross-sectional sample shown in Fig. 12 (courtesy of Professor Munz, Sheffield Hallam University, U.K.)

Table 2 Cutting tool life experimental results

Cutting tool	Spindle speed, m/min	Cutting tool life
Uncoated tool (WC-Co)	30	1 min
	50	9 s
	70	3 s
TiN-coated WC-Co	30	1.5 min
	50	16.5 s
	70	5 s
$Ti_{0.46}Al_{0.54}N$-coated WC-Co	30	2 min
	50	27 s
	70	10.5 s
$Ti_{0.44}Al_{0.53}Cr_{0.03}N$-coated WC-Co	30	2.5 min
	50	37 s
	70	15 s
$Ti_{0.43}Al_{0.52}Cr_{0.03}Y_{0.02}N$-coated WC-Co	30	3.9 min
	50	63 s
	70	27 s

The STEM-EDX compositional profiles across grain boundaries in annealed $Ti_{0.44}Al_{0.50}Cr_{0.04}Y_{0.02}N$ films show a significant segregation of Y. An example, corresponding to the line-labeled A-A in Fig. 12(c), is reproduced in the upper left-hand corner of Fig. 12. The concentration profile of Y at the boundary is enhanced more than a factor of two. The presence

Table 3 Tool life, cutting speed, constants derived for various materials using uncoated carbide tools after Kronenberg's monograph on machining science

Composition of workpiece		Cutting speed, v		Tool life		C_{VR}(*)		Tool life exponent
Pearlite, %	Ferrite, %	ft/min	m/min	in.^{3} T_{vol}	min T_b	ft/min	m/min	y
10	90	785	240	400	42.5	852	260	0.342
		850	259	300	29.4			0.342
		1000	305	225	18.7			0.342
30	70	520	159	400	64	660	200	0.336
		580	176	300	43			0.336
		710	216	200	23.5			0.336
		1000	305	100	8.33			0.336
Spheroidized		300	91.5	380	106	492	150	0.388
		510	156	200	32.8			0.388
		1000	305	60	5.0			0.388
50	50	300	91.5	275	76	460	140	0.400
		660	202	100	12.6			0.400
		1000	305	50	4.15			0.400
100	0	300	91.5	190	53.7	394	120	0.404
		800	243	50	5.2			0.404
		1000	305	37	3.1			0.404

of excess Y and YO_x at the film grain boundaries may play a decisive role in reducing bulk film oxidation rates through the inhibition of both cation out-diffusion and O in-diffusion.

3.3 Cutting Tool Life and Wear Behavior

The lives of the uncoated and coated cutting tools were compared after measuring the progression of the flank wear of the cutting tool inserts after machining at different cutting speeds under the previously stated conditions. The results of the tool-life experiments are presented in Table 2. Under these machining conditions, the dominant wear behavior observed during the machining experiments was flank wear.

The data provided above allow the calculation of the Taylor tool life for each cutting tool type for the experimental conditions stated. The following equations relate to the cutting tool types described:

- Uncoated WC-Co $VT^{0.28} = 30$
- TiN coated WC-Co $VT^{0.3} = 34$
- $Ti_{0.46}Al_{0.54}N$ coated WC-Co $VT^{0.35} = 38$
- $Ti_{0.44}Al_{0.53}Cr_{0.03}N$ coated WC-Co $VT^{0.37} = 42$
- $Ti_{0.43}Al_{0.52}Cr_{0.03}Y_{0.02}N$ coated WC-Co $VT^{0.39} = 51$

The results presented show that the tool life is increased as the coating was improved with small additions of elemental Cr and Y. This effect coincides with the observations on the oxidation behavior of the coatings that were treated with various elemental concentrations of Cr and Y. Compared with other materials, the tool-life equations appear to show that the machining of uranium alloys results in an extremely low tool life compared with more commonly used engineering steels with microstructures that tend to favor good machinability. A selection of tool life constants for more commonly used engineering materials is shown in Table 3 and is taken from Kronenberg's book on machining science and application (Ref 17).

The machinability of uranium alloys appears to be similar to that of austenitic stainless steels (i.e., very low tool life even at moderately high cutting speeds). The observations of wear behavior tend to show that the normal mode of wear during machining is progressive flank wear. However, it must be noted that the experiments on cutting tool life were based on roughing machining conditions and did not include an experimental determination of tool life during finish machining.

4. Conclusions

The incorporation of 3 mol% CrN in $Ti_{1-x}Al_xN$ alloys did not significantly change film hardness or microstructure. The latter remained columnar with individual columns consisting of single grains over extended vertical distances. Adding an additional 2 mol% YN increased the film hardness by $HK_{0.025}$ ≈300 kg/mm^2, while Y segregation during growth promoted continuous renucleation, which resulted in considerable grain refinement and a more equiaxed structure.

Thermogravimetric analysis in oxidizing ambient atmospheres showed that the onset of rapid oxidation was increased from ≈600 °C for TiN to 950 °C for $Ti_{0.43}Al_{0.52}Cr_{0.03}Y_{0.02}N$, compared with 870 °C for $Ti_{0.46}Al_{0.54}N$ and 920 °C for $Ti_{0.44}Al_{0.53}Cr_{0.03}N$. The initial oxidation reaction path was found to be similar for the three alloys with the formation of an Al-rich surface oxide and Ti-rich oxide underlayer. Annealing $Ti_{0.44}Al_{0.53}Cr_{0.03}N$ layers on steel substrates for 1 h at 950 °C results in massive oxidation with cation out-diffusion and gives rise to void formation and underdense column boundaries extending nearly to the film-substrate interface. Voids are also observed on the substrate side of the film-substrate interface due to the rapid out-diffusion of Cr, which is rejected by Ti-rich sublayers in the oxidized film and accumulates at adjacent boundaries, and Fe. In stark contrast, the addition of only 2 mol% YN to form $Ti_{0.43}Al_{0.52}Cr_{0.03}Y_{0.02}N$ reduces the oxide thickness from >3 to ≈0.4 μm while significantly inhibiting out-diffusion of substrate species. The STEM-EDX profiles obtained after annealing show that Y segregates to the nitride grain boundaries. This may explain the enhanced high-temperature oxidation resistance of the $Ti_{0.43}Al_{0.52}Cr_{0.03}Y_{0.02}N$ alloy as Y and YO_x inhibit grain-boundary diffusion of both cation species toward the free surface and oxygen penetration into the film. The machining characteristics of coated cutting tools had some benefit in extending the life of the cutting tool when machining uranium alloys. The benefits associated

with using Ti-base coated tools were further enhanced by using a superlattice-coated cutting tool. This ensured that thermal fatigue cracking of the coating did not interfere with the normal operation of the cutting insert when machining uranium alloys. The use of coated tools appeared to make for a tool life that was similar to that provided by the use of austenitic stainless steels. However, further experiments are required to determine the life of the tools when finish machining operations are involved.

References

1. Tool Wear, *Modern Metal Cutting: A Practical Handbook*, Sandvik-Coromant, 1994, p 1-27
2. J.A Aris, Machining of Uranium and Uranium Alloys, *Machining*, Vol 16, ASM Handbook (formerly, *Metals Handbook*, 9th ed.), ASM International, 1989, p 874-878
3. O. Knotek, M. Böhmer, and T. Leyendecker, Structure and Properties of Ti and Al Hard Compound Films, *J. Vac. Sci. Technol., A,* 1986, **4,** p 2695-2710
4. H. Jehn, S. Hofmann, V.-E. Rückborn, and W.-D. Münz, Morphology and Properties of Sputter (Ti,Al) N Layers on High-Speed Steel as a Function of Deposition Temperature and Sputtering Atmosphere, *J. Vac. Sci. Technol., A,* 1986, **4,** p 2701-2705
5. W.-D. Münz, TiAlN Films: An Alternative to TiN Coatings, *J. Vac. Sci. Technol., A,* 1986, **4,** p 2717-2725
6. G. Håkansson, J.-E. Sundgren, D. McIntyre, J.E. Greene, and W.-D. Münz, Microstructure and Physical Properties of Polycrystalline Metastable Ti0.5Al0.5N Alloys Grown by d.c. Magnetron Sputter Deposition, *Thin Solid Films,* 1987, **153,** p 55-62
7. D. McIntyre, J.E. Greene, G. Håkansson, J.-E. Sundgren, and W.-D. Münz, Oxidation of Metastable Single Phase Polycrystalline Ti0.5Al0.5N Films, *J. Appl. Phys.,* 1990, **67,** p 1542-1553
8. W.-D. Münz, Oxidation Resistance of Hard Wear Resistant Ti0.5Al0.5N Coatings Grown by Magnetron Sputtering Deposition, *Werkstoffe Korros.,* 1990, **41,** p 753-754
9. W.-D. Münz, D. Schulze, and F.J.M. Hauzer, A New Method for Hard Coatings: Arc Bond Sputtering, *Surf. Coat. Technol.,* 1992, **50,** p 169-178
10. I. Petrov, P. Losbichler, D. Bergstrom, J.E. Greene, W.-D. Münz, T. Hurkmans, and T. Trinh, Large Scale Fabrication of Hard Superlattice Films by Combined Stress Arc Evaporated Unbalanced Magnetron Sputtering, *Thin Solid Films,* 1997, **302,** p 179-192
11. W.-D. Münz, I.J. Smith, D.B. Lewis, and S. Creasey, Droplet Formation on Steel Substrates During Cathodic Arc Steered Metal Ion Etching, *Vacuum,* 1997, **48,** p 473-481
12. J.W. Colby, *Qauntex-ray Instruction Manual,* Kevex, Foster City, CA, 1980
13. JCPDS International Center for Powder Diffraction Data, *Powder Diffraction File for TiN [6-642]*, JCPDS International Center for Powder Diffraction Data, Swarthmore, PA, 1989
14. I. Petrov, L. Hultman, U. Helmersson, J.-E. Sundgren, and J.E. Greene, A Newly Developed Ion Implanter for Industrial Applications, *Thin Solid Films,* 1989, **169,** p 299-314
15. F. Adibi, I. Petrov, L. Hultman, U. Wahlström, T. Shimizu, D. McIntyre, J.E. Greene, and J.-E. Sundgren, Low Energy Ion Irradiation During Growth of TiN, *J. Appl. Phys.,* 1991, **69,** p 6437-6450
16. VDI-Richtlinien 3198, *Beschichten von Werkzeugen der Kkaltmassivumformung,* Beuth Verlag, Berlin, Germany, 1992
17. M. Kronenberg, *Machining Science and Application,* Pergamon Press, Oxford, U.K., 1996